Research Square

Preprints are preliminary reports that have not undergone peer review.
They should not be considered conclusive, used to inform clinical practice,
or referenced by the media as validated information.

Removal of chloroquine phosphate by ultrafine cobalt nanoparticles in peroxymonosulfate activation

haoran guo
Ningxia Normal University
zixuan xu
Ningxia Normal University
jiapeng wang
Ningxia Normal University
tiaobin zhao
Ningxia Normal University
hui xu
Ningxia Huayu Chemical Co., Ltd.
haijiao xie
Hangzhou Yanqu Information Technology Co., Ltd.
xiaoni qi
Ningxia Normal University
zhenliang li
1051289681@qq.com
Ningxia Normal University

Research Article

Keywords: Chloroquine phosphate, N-doped biochar, Peroxymonosulfate, Photocatalysis

Posted Date: March 30th, 2026

DOI: https://doi.org/10.21203/rs.3.rs-9051938/v1

License: This work is licensed under a Creative Commons Attribution 4.0 International License.
Read Full License

Additional Declarations: No competing interests reported.

Removal of chloroquine phosphate by ultrafine cobalt nanoparticles in peroxymonosulfate activation

Abstract

The ultrafine cobalt nanoparticles (CoNPs) are among the best materials for photocatalysis. Co/NC, derived from turnip as a raw material using plant cells as templates and pyrolyzed at 400 °C, features highly dispersed 3-5 nm CoNPs embedded in N-doped biochar. The CoNPs with exposed (111)-dominated facets, enable both radical and non-radical peroxymonosulfate (PMS) activation, leading to the highly efficient degradation of 50 mL of chloroquine phosphate (CQP) within 10 minutes under UV-visible light in various water matrices, including river water, reservoir water, and tap water. Density functional theory (DFT) calculations confirmed that the (111)-dominated facets, which serve as the active centers, tend to attack the peroxide bond (O-O) of PMS. Notably, the degradation efficiency of CQP, tetracycline (TC), methyl orange (MO), doxycycline hydrochloride (DH), oxytetracycline (OTC), congo red (CR), and methylene blue (MB) by Co/NC-7/PMS was evaluated in natural water. Additionally, the degradation performance of the above organic pollutant mixture was assessed. Both •OH, $^1O_2$, and $O_2^{\bullet-}$ were confirmed to be the main reactive oxygen species (ROS) participating in the photocatalytic degradation of CQP. The plausible degradation pathways of CQP were also deduced based on the degradation intermediates identified by HPLC-MS analysis.

Keywords Chloroquine phosphate, N-doped biochar, Peroxymonosulfate, Photocatalysis

1. Introduction

Recently, adsorption, chemical degradation and biological treatment were the main techniques to treat the organic pollutants in the aquatic environment [1]. The advanced oxidation process (AOPs) based on the sulfate radical have been proven to be the effective methods to degrade organic pollutants due to the higher efficiency. Compared with traditional hydroxyl radical-based AOPs (•OH: redox potential of 1.8-2.7 V vs. NHE and half-life of 20 ns), sulfate radical ($SO_4^{\bullet-}$: 2.5-3.1 V vs. NHE) has longer life-span (30−40 μs), and a broader applicable pH range (pH=2-9). Besides, their high reactivity and oxidation capability of a wide range of different types of pollutant [2]. Currently, many ways were reported to activate peroxymonosulfate and peroxydisulfate (PDS), which included the heat, UV light, microwave irradiation, transition metal-based materials, and base activation [3]. Among the commonly studied transition metals (M = Co, Fe, Mn, and Cu), Co has been considered as the most effective activators of PMS due to its higher standard redox potential [4]. The ultrafine cobalt nanoparticles (U-CoNPs) as catalysts with the maximum atomic utilization and ample active centers have attracted more attentions. Furthermore, Co^0 can not only activate PMS to produce $SO_4^{\bullet-}$, but also reduce Co^{3+} to Co^{2+}. Co nanoparticles were immobilized on the N-doped biochar for sulfanilamide degradation, as the results indicated that the sulfanilamide could be decomposed within 5 min during the first three cycles [5]. Recently, carbon-based materials such as activated carbon, carbon nanotubes, reduced graphene oxide, and biochar have been identified as metal-free alternatives for activating PMS. Notably, biochar has rapidly emerged as a promising activator due to its low preparation cost and abundant sources. [6],[7]. The new type of biochar derived from food waste was prepared by Jinping Li, which was the excellent activator of PDS for reactive red X-3B degradation due to its unique characteristics [8]. Virender K. Sharma has proposed a strategy for degrading the humic acids in water using microwave irradiation assisted by persulfate

and activated carbon. The higher removal efficiency may be attributed to the enhanced generation of $SO_4^{\bullet -}$ and •OH radicals [9].

The original biochar exhibited low catalytic activity. However, after modification (specifically through N-doping), the biochar demonstrated outstanding catalytic performance. Indeed, N-doping has been widely recognized as an effective strategy for enhancing the catalytic performance of carbon-based materials[10]. Furthermore, the incorporated nitrogen dopants facilitate the generation of ROS by activating peroxymonosulfate (PMS). [11]. The pyridinic-N, pyrrolic-N and graphitic-N were identified as the potential activators of PMS. For instance, pyridinic N serves as adsorption site to immobilize PMS. Thereby weakening the peroxide bond (O-O), this facilitates electron transfer from the pyridinic-N to PMS, leading to the generation of sulfate radicals($SO_4^{\bullet -}$). Graphitic-N, on the other hand, promotes the production of singlet oxygen ($^1O_2$) through the interfacial interaction between PMS and the N-doped carbon matrix. [12]. Haipeng Wu prepared nitrogen-doped, graphitic biochar fibers from Boehmeria nivea [13]. This modified biochar exhibited a tetracycline degradation rate approximately seven times higher than that of the original biochar, which was attributed to the graphitic structure and nitrogen doping synergistically accelerating electron transfer [14]. Separately, Fanghua Liu synthesized Co_3O_4-loaded biochar as a peroxymonosulfate (PMS) activator for chloramphenicol degradation [15]. The biochar/Co_3O_4 composite demonstrated a synergistic photocatalytic effect, where the biochar component likely facilitated electron transfer between Co species and PMS, thereby promoting the Co^{2+}/Co^{3+} redox cycle. In another study, N-doped biochar-supported U-CoNPs were confirmed as an efficient PMS activator for CQP degradation [16]. Catalyst morphology also influences the selectivity of reactive oxygen species generation. Besides, Hexin Zhang and co-workers reported nanorod-like Co_3O_4 with (110) plane exposed exhibiting a superior activity for PMS activation to efficiently remove bisphenol A in water[17]. Huan Wang synthesized Co_3O_4 nanoparticles of different morphologies with predominantly exposed (001), (111), and (112) facets. This study systematically elucidates the influence of Co_3O_4 crystal facets on $^1O_2$ generation[18]. Therefore, facet-dependent ROSs generation behaviors have attracted more and more attentions [19,20].The inner tissue of white radish contains abundant plant cells, which store water and nutrients. The cell wall, a key structural component, protects these cells. Inspired by this natural structure, this study aimed to construct a low-cost photocatalyst by embedding ultrasmall cobalt nanoparticles (U-CoNPs) into a nitrogen co-doped biochar (Co/NC-74) with exposed (111) facets. Specifically, Co/NC-74 was synthesized using turnip-derived plant cells as a template. For the first time, this plant cell template was employed to confine and control the size of nanoparticles for activating peroxymonosulfate (PMS) to degrade chloroquine phosphate. Using $Co(NO_3)_2$ as the source of both cobalt and nitrogen, the Co/NC-74 composite was obtained through freeze-drying followed by pyrolysis under a N_2 atmosphere. The embedded ultrafine CoNPs were expected to provide more active sites. Moreover, the metallic cobalt (Co^0) derived from ultrafine CoNPs could activate PMS. This plant cell templating method is envisioned to provide a novel strategy for constructing high-performance Co/NC-74 photocatalysts.

2. Experimental

2.1. Materials

Potassium peroxymonosulfate (PMS, $KHSO_5 \cdot 0.5KHSO_4 \cdot 0.5K_2SO_4$), cobalt nitrate hexahydrate ($Co(NO_3)_2 \cdot 6H_2O$), p-benzoquinone (PBQ), chloroquine phosphate (CQP), doxycycline hydrochloride (DH), methanol (MeOH), oxytetracycline (OTC), tetracyclines (TC), methyl orange

(MO), congo red (CR), methylene blue (MB), Metanil yellow (MY), potassium peroxymonosulfate (PMS, $KHSO_5 \cdot 0.5KHSO_4 \cdot 0.5K_2SO_4$), furfuryl alcohol (FFA), L-isopropyl alcohol (IPA), and ethyl alcohol (EtOH) were purchased from Macklin reagent Co., Ltd. Radish as raw material was purchased from Renrenjia super market in Guyuan city.

2.2. Synthesis of Co/NC

The synthesis of Co/NC involved a cell-template-based approach using white turnip as the raw material. The first step was the preparation of dehydrated shredded turnip. The shredded turnip was immersed in a $Co(NO_3)_2$ solution under vigorous magnetic stirring. Subsequently, the product was freeze-dried and then subjected to high-temperature pyrolysis. A series of samples were prepared with 5, 6, 7, and 8 mmol of $Co(NO_3)_2$[21]. The catalysts subjected to pyrolysis at 300 °C, 400 °C, and 500 °C were denoted as Co/NC-73, Co/NC-74, and Co/NC-75, respectively.

2.3. Characterization

The crystalline phases of the different samples were measured with X-ray diffraction (XRD, Rigaku Ultima IV, Japan) with Cu-Kα radiation. X-ray photoelectron spectroscopy (XPS, ESCALAB 250Xi, America) was carried out to measure the surface chemical state and valence bands of samples. The morphology and microstructure of samples were analyzed by Scanning Electron Microscopy (SEM, Carl Zeiss Bruker 6/30, Germany) and the high-resolution transmission electron microscopy (HRTEM, JEM-2100, JEOL, Japan). Brunauer-Emmett-Teller (BET) specific surface area of samples were analyzed by multi-channel automatic surface area and porosity analyzer (Micromeritics TriStar II 3020, America).

2.4. Evaluation of catalytic performance

The analytical methods of samples were provided in the Supplementary Material.

2.5. Computational details

More DFT calculation could be found in the Supplementary Material.

3. Results and discussion

3.1. Characterization

3.1.1. XRD and XPS analysis

The X-ray diffraction (XRD) pattern of Co/NC-74 is presented in Fig. 1a. It shows three distinct peaks at 44.3°, 51.6°, and 75.8°, which can be indexed to the (111), (200), and (220) lattice planes of metallic Co, respectively [22]. X-ray photoelectron spectroscopy (XPS) confirmed that C, O, N, and Co are the primary elements in Co/NC-74(Fig. 1b). As shown in Fig. 1c, the C 1s spectrum can be deconvoluted into three peaks at 284.8 eV (C–C), 286.1 eV (C=N/C–N), and 289.1 eV (C=O) [23], indicating the successful introduction of nitrogen into the carbon matrix. The Co 2p spectrum (Fig. 1d) reveals the coexistence of metallic Co and Co(II) species. The presence of Co(II) possibly generated from the surface oxidation of metallic cobalt nanoparticles upon air exposure[24]. The high-resolution N 1s spectrum (Fig. 1e) was fitted with three peaks at 398.3 eV, 399.0 eV, and 400.0 eV, corresponding to pyridinic N, graphitic N, and other nitrogen species, respectively [25]. Furthermore, the O 1s spectrum (Fig. 1f) displays two main peaks at 531.4 eV and 532.7 eV, assigned to surface hydroxyl groups (O_{ads}) and adsorbed water (O_w), respectively [26]. This confirms the presence of hydroxyl groups on the surface of Co/NC-74.

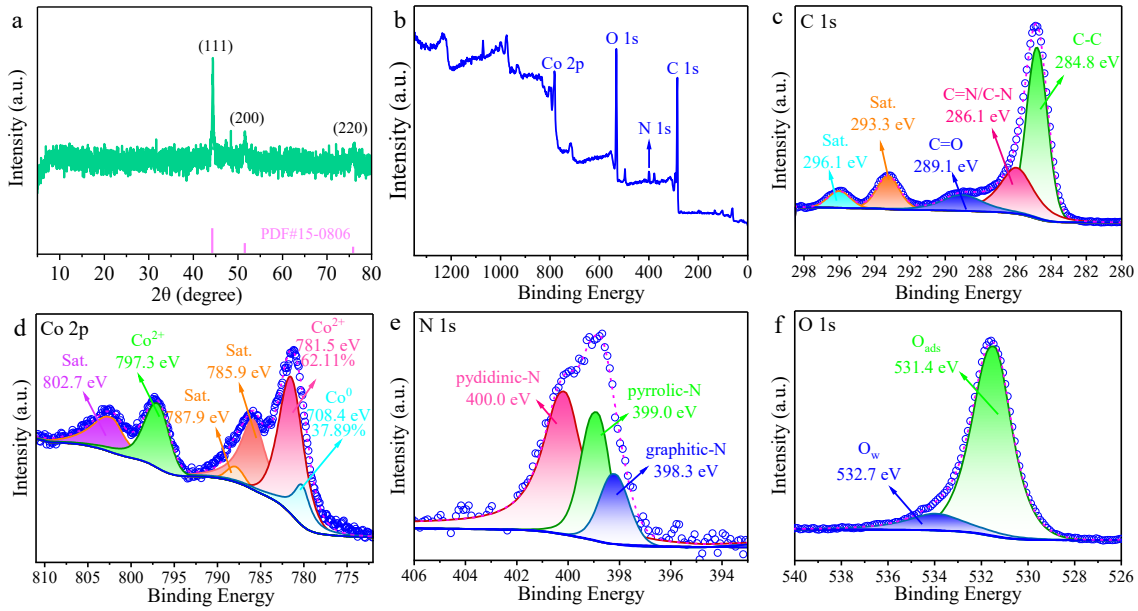


Fig. 1. XRD patterns (a) and XPS spectra of Co/NC-74, (b) total survey, (c) C1 s, (d) Co 2p, (e) N1 s, and (f) O 1 s.

3.1.2. SEM and TEM analysis

Procedure for the preparation of the Co/NC-74 was presented in Fig. 2a. The specific surface area and pore structure of Co/NC-74 were investigated using N_2 adsorption-desorption measurements (Fig. 1S). The isotherm of Co/NC-74 was consistent with a Type IV curve featuring an H3 hysteresis loop, indicating a mesoporous structure. The pore size distribution was primarily in the range of 5–20 nm [27], and the specific surface area was measured to be 4.34 m^2/g. This porous structure and large surface area facilitate the distribution of active sites, thereby increasing the contact efficiency between the catalyst and pollutants. The surface morphology of Co/NC-74 was analyzed by SEM and TEM (Fig. 2b). The images show that Co particles were evenly distributed and anchored on the surface of the N-doped biochar (NC). This good dispersion is favorable for peroxymonosulfate (PMS) activation, as it provides more exposed reactive sites. TEM images further revealed that ultrafine cobalt nanoparticles were uniformly dispersed, with an average particle diameter of approximately 5.64 nm (Fig. 2c). As shown in the HRTEM image (Fig. 2d), clear lattice fringes with an interplanar spacing of 0.203 nm were observed, corresponding to the (111) crystal planes of metallic Co[28]. Furthermore, elemental mapping images (Fig. 2e-h) confirmed the homogeneous distribution of C, O, N, and Co, providing additional insight into the spatial arrangement of the nanocomposite and indicating the successful incorporation of Co and N into the NC framework.

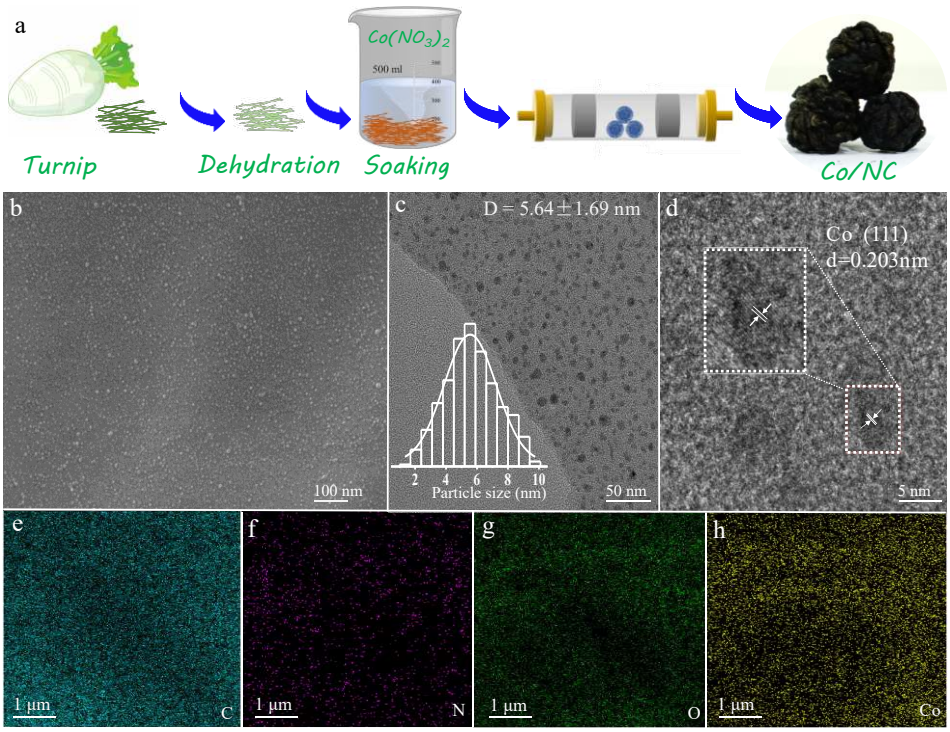


Fig. 2. Schematic illustration of the synthetic procedures for Co/NC-74 (a), SEM images (b), TEM images(c, d) and the elemental mapping images (e-h).

3.2. Study on preparation conditions

The influence of the Co^{2+} concentration on the catalytic performance of Co/NC was evaluated. Dehydrated fresh shredded radish was used to prepare catalysts with Co^{2+} solutions of different concentrations. The catalytic reactivity of catalysts were investigated. CQP was hardly decomposed by PMS, which exhibited slight catalytic performance on CQP, with a removal efficiency of only 1.06%. CQP was hardly degraded under visible light illumination in absence of catalyst, indicating that the degradation of CQP was motivated by the Co/NC-74. Notably, when the Co/NC was prepared with 7 mmol $Co(NO_3)_2$, which was confirmed to be the superior catalyst, by which the removal efficiency reaches 100% within 10 min (Fig. 3a). The results indicated that the Co^{2+} can remarkably affect the degradation of CQP. It is widely known that the inner body of natural radish contains abundant plant cells which can store water and nutrients for growth. The cell wall is a key component of white radish that protects these cells. Herein, to further explore an efficient way for facilitating the entry of Co ions into radish cells, we took advantage of the fact that radish cells can rapidly reabsorb water after dehydration, allowing cobalt solution to penetrate simultaneously(Fig. 2S). For comparison, the degree of dehydration was controlled artificially based on mass ratio. The fresh shredded radish with different dehydration were immersed into 7 mmol Co solution for 2 h to prepare catalyst. After drying, the material was used to prepare Co/NC at 500 ℃ in N_2. When 25% of the water was removed from the radish cells for preparing catalyst, the resulting catalyst decomposed CQP in 4 min. These results indicate that Co^{2+} can enter plant cells more readily after partial dehydration. This work further evaluated the effects of pyrolysis temperature on CQP degradation in Fig. 3b. The optimized catalyst Co/NC-74 achieved complete (99.99 %) removal of CQP within 6 min. Under ultraviolet and visible light irradiation. The Co/NC-73 reached 89.16 % of degradation efficiency under ultraviolet and visible light irradiation. Besides, the Co/NC-75 degrades 97.38 % of CQP within 10 min. These results could correspond to the phase transformation

of catalyst at 400 ℃ [29].

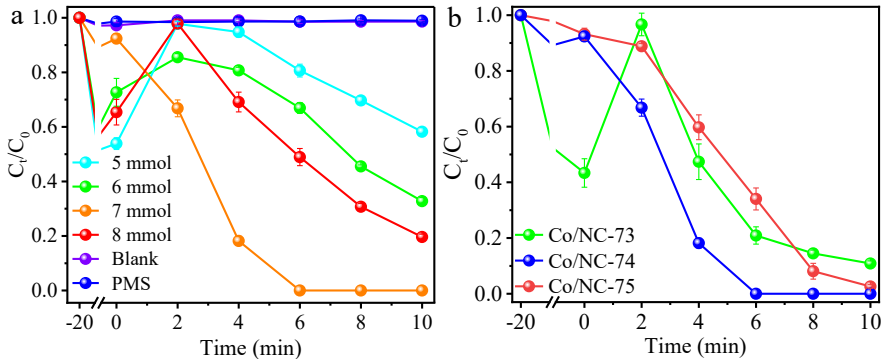


Fig. 3. The effects of (a) Co^{2+} concentration and (b) pyrolysis temperature.

3.3. Effects of reaction parameters on CQP degradation

3.3.1. Effects of catalysts dosage and PMS concentration

The influence of reaction parameters including catalyst dosage and PMS concentration were evaluated during the CQP degradation by Co/NC-74 catalyst [30]. When the dosage of Co/NC-74 was increased from 10 to 20 mg, the removal efficiency of CQP increased from 77.10 % to 99.98 % (Fig.4a). Additionally, to further raising Co/NC-74 dosage, the degradation efficiency of CQP decreased slightly. Therefore, excessive increasing the dosage of Co/NC-74 has hardly enhanced the removal efficiency of CQP. The optimum dosage of Co/NC-74 was 20 mg and was applied in the subsequent experiments.

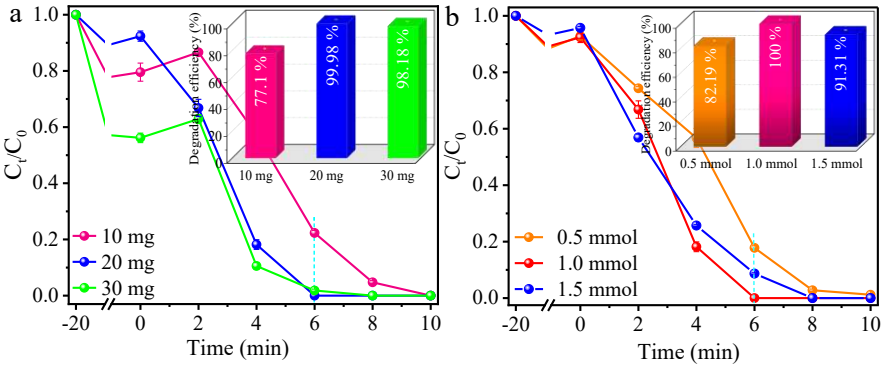


Fig. 4. Effects of catalysts dosage (a) and PMS concentration (b) (inset: the degradation efficiency of CQP at 6 min).

3.3.2. Effects of solution pH

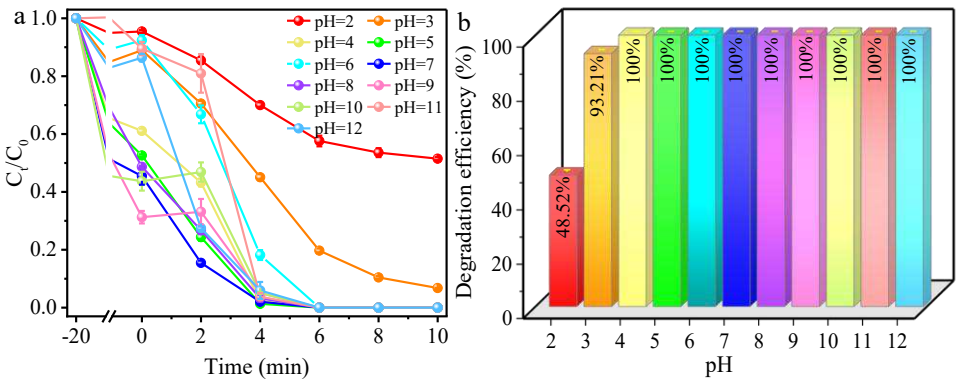


Fig. 5. The effects of pH on CQP degradation: (a) line chart (b) bar graph.

The initial pH of the reaction solution was identified as another key factor affecting CQP degradation, as shown in Fig. 5. The degradation experiments were conducted across a pH range of 2 to 12. Within 10 minutes, CQP removal efficiency rose sharply from 48.52% to 100% as pH increased from 2 to 4. Furthermore, removal efficiency remained at 100% in the pH range of 4 to 12, indicating that CQP can be degraded effectively across nearly the entire pH range studied. Generally, a large number of H^+ ions not only promotes the generation of ROSs [31], but also enhances the reduction potential of Co^{3+} during the reaction process [32]. These results indicated that the Co/NC-74 can degrade CQP rapidly and efficiently over a broad pH range.

3.4. The potential mechanism of CQP degradation by Co/NC activated PMS

3.4.1. Identification of ROSs in Co/NC/PMS system

It was essential to identify which ROSs were really present and involved in the CQP degradation process activated by Co/NC-74/PMS. A series of ROSs quenching experiments were conducted to verify their presence in the Co/NC-74/PMS system, as shown in Fig.6. Typically, methanol (MeOH) and isopropanol (IPA) are common scavengers for the •OH[33]. MeOH can quench both •OH and $SO_4^{\bullet -}$ [34], whereas IPA primarily quenches •OH due to the faster reaction rate with •OH compared to $SO_4^{\bullet -}$ [35]. Upon adding MeOH from 1.0 mM to 5.0 M, the CQP degradation efficiency dropped sharply from 99.80 % to 71.58 % (Fig.6a). Similarly, with the addition of IPA from 0.1 to 3.0 mM, the CQP removal efficiency decreased from 89.42% to 46.83 % (Fig.6b). These results suggested that both •OH and $SO_4^{\bullet -}$ participated in the CQP degradation. Compared to the $SO_4^{\bullet -}$, the contribution of •OH was significant for CQP degradation over the Co/NC-74/PMS system. In addition, p-benzoquinone (PBQ) and furfuryl alcohol (FFA) were used as ROSs scavenger for $O_2^{\bullet -}$ and $^1O_2$, respectively [36]. The presence of FFA notably inhibited the CQP degradation (Fig.6c), meanwhile a significant inhibitory effect was observed with PBQ (Fig.6d) [37]. The results indicated that the coexistence of $O_2^{\bullet -}$ and $^1O_2$ in the Co/NC-74/PMS system. Thus, both $^1O_2$ and $O_2^{\bullet -}$ have an equally important contribution to the removal process of CQP. However, quenching experiments alone do not provide fully reliable identification of ROSs. Thus,electron paramagnetic resonance (EPR) tests was further used to verified the ROSs involved in the Co/NC-74/PMS system. As seen in Fig. 7a, the characteristic peaks revealed that the existence of •OH and $SO_4^{\bullet -}$ in the degradation process of CQP. In addition, the weak signals of DMPO-$SO_4^{\bullet -}$ were observed, which indicated that the EPR results were inconsistent with the free radical quenching test. Besides, the strong signals of TEMP-$^1O_2$ (Fig.7b)and DMPO-$O_2^{\bullet -}$ (Fig.7c) were detected in the Co/NC-74/PMS system [38,39], revealing the involvement of $^1O_2$ and $O_2^{\bullet -}$ in the CQP degradation process. The EPR results and free radical quenching experiments indicated that the CQP degradation in the Co/NC-74/PMS system through free radical and non-radical pathways. Among the ROSs, •OH, $^1O_2$ and $O_2^{\bullet -}$ play major roles [40,41]. For the purpose of further investigating the mechanism of Co/NC-74 on PMS activation, DFT calculations were performed. When the PMS molecular reached up to Co/NC-74, Co could coordinate with various O atoms of PMS, which were oriented perpendicular to the 2D plane of Co/NC-74. The adsorption energy (E_{ads}) and O-O bond lengths (L_{O-O}) for the adsorption of 1 O, 2 O and 3 O in PMS on Co sites were observed in Fig. 7d, Upon binding of the Co atom to the 2 O and 3 O site of PMS, the E_{ads} were respectively -0.73, -1.86 eV. Moreover, the L_{O-O} increased after the PMS adsorption (the L_{O-O} of original PMS was 1.453 Å), revealing that a lower E_{ads} and a longer L_{O-O} on 2 O and 3 O of PMS [42]. This further confirmed that 2 O and 3 O were the primary active sites, which was consistent with EPR test.

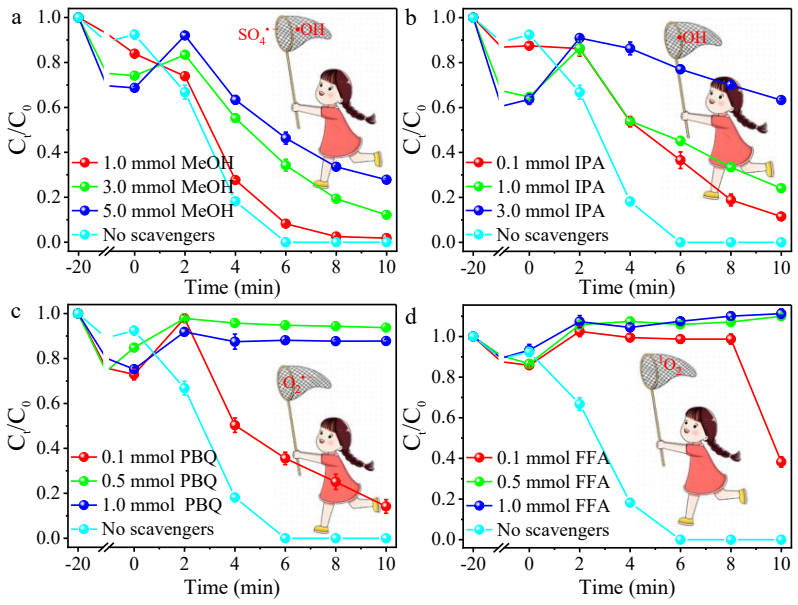


Fig.6. The effects of (a)IPA, (b) MeOH, (c) FFA, and (d) PBQ inhibitory effect on the CQP degradation.

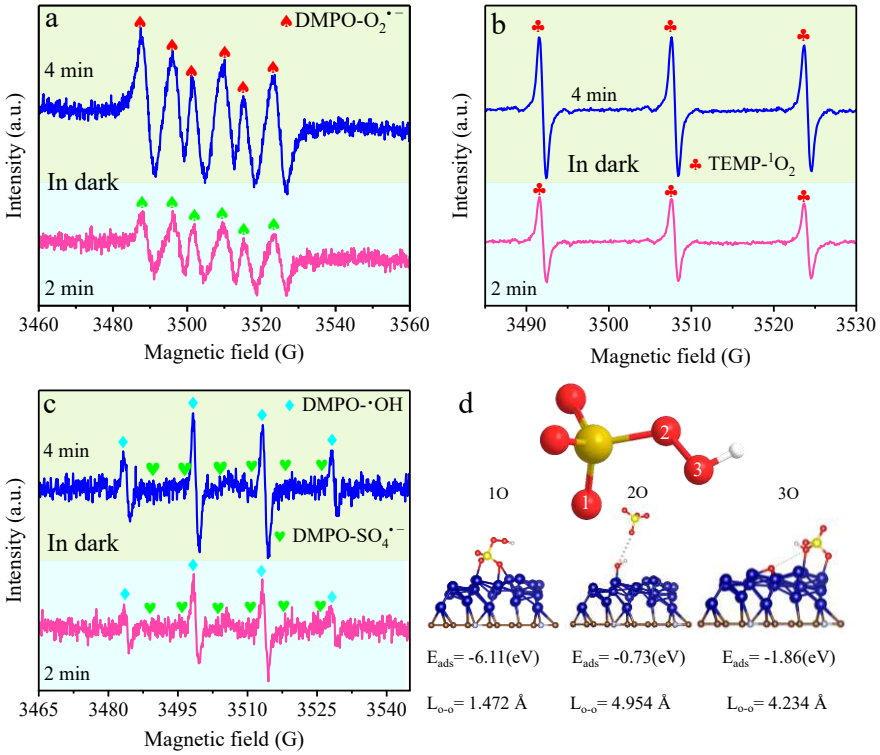
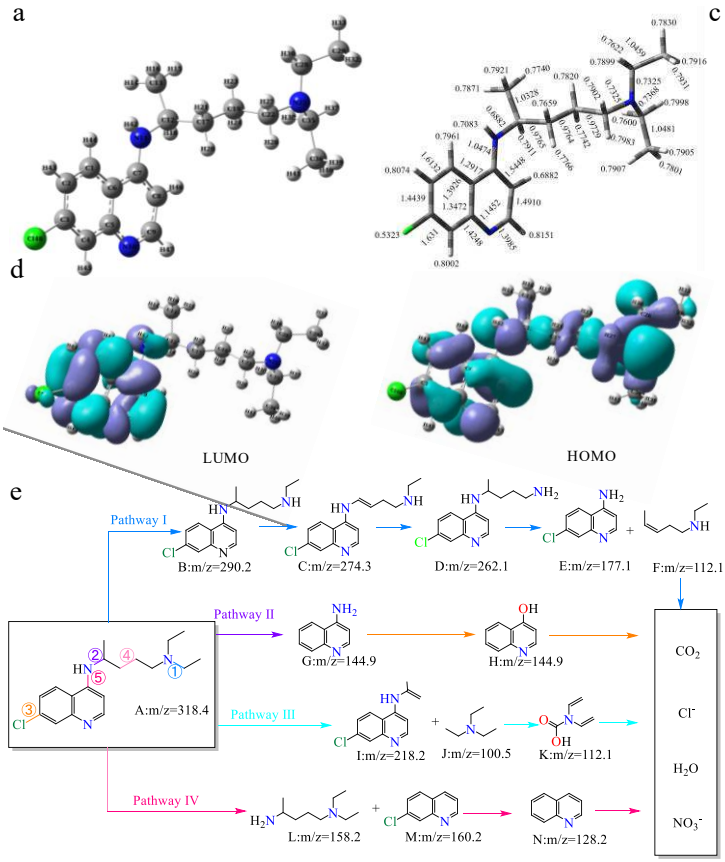


Fig. 7. EPR spectra of PMS activation by Co/NC-74 with DMPO (a, c) and TEMP (b) as the spin-trapping reagents; possible reaction model of Co/NC-74 and PMS.(d) Adsorption model of catalyst and PMS.

3.5. Degradation pathways of CQP

The DFT-based Fukui index calculations are applied to evaluate the reactive sites of CQP that are subject to both non-radical and radical attacks. The molecular structure of CQP was displayed in Fig. 8a. The higher electrophilic (f^-) and nucleophilic (f^+) indices of CQP atoms suggested that it would be attacked by electrophilic species ($^1O_2$ and h^+), nucleophilic species ($O_2^{\bullet-}$), and radical species ($SO_4^{\bullet-}$ and ·OH), respectively [43]. The Laplacian bond order (LBO) was utilized for predicting the bond break positions, the primary dates can be found in Table 1S, the bond order of

48Cl-3C was found to be the lowest at 0.5323 in Fig. 8b, suggesting that it may exhibit the highest susceptibility to chemical bonds breakage [44, 45]. Additionally, the lower LBO values for the 11 N – 12C and 25 N – 28C bonds indicate that these bonds are more likely to break during the degradation reaction. The Fukui index was used to investigate the electrophilic and free radical attack in Fig. 8c. For CQP, N25 (f^-=0.1043, f^0 =0.0538), N10 (f^-=0.0661, f^0 =0.0663), and N11 (f^-=0.0615, f^0 =0.0471), the relatively high Fukui indices suggested that they are most likely to be attacked by the electrophilic reagents and free radicals. Furthermore, the highest occupied molecular orbital (HOMO) analysis further corroborated these findings, indicating the regions that are most likely to release electrons [46]. As shown in Fig. 8d, the HOMO of CQP was primarily concentrated on the N-heterocyclic ring, and N atoms. It is reasonable to assume them are susceptible to be attacked by electrophilic radicals (h^+). Conversely, the LUMO of CQP primarily localized on the benzopyridine ring, rendering them more vulnerable to free radical ($O_2^{\bullet -}$) attack [47]. In this work, although the removal efficiency of CQP in Co/NC-74/PMS catalytic system was near to 100 %, part of the CQP was converted to other intermediates [48]. The degradation pathways of CQP were investigated with liquid chromatography-mass spectrometry (LC-MS). The potential CQP transformation in Co/NC-74/PMS exhibited four pathways. In the pathway 1, 7-chloroquinolin-4-amine was obtained due to the broken C-N bond (labelled as 2) in the chain branches. Finally, the small molecular was converted into intermediates through the ring-opening reaction. In the pathway II, CQP molecules were converted to G (m/z = 144.9) and H (m/z = 144.9) after the cleavage of C-N bond (labelled as 2) and C-Cl bond (denoted as 3). Further oxidative cleavage of the piperazine ring, G and H underwent mineralization. In the pathway III, CQP molecules undergoes breakdown of C-C bond (labelled as 4) forming I (m/z = 218.2) and J (m/z = 112.1). Subsequent cleavage of CQP's pyridine ring, which are further oxidized by ROSs into smaller molecules. In the pathway IV, the oxidation effect of ROSs can lead to the conversion of CQP molecules to L (m/z = 158.2) and M (m/z = 160.2) after the C–C bond cleavage. Quinoline N (m/z = 218.2) can be observed after the dechlorination reaction. After degradation progresses, these intermediate products are further mineralized into simpler molecules.



Atom	q(N)	q(N+1)	q(N1)	f⁻	f⁺	f⁰	CDD
1(C)	0.0426	0.1272	0.0205	0.0221	0.0847	0.0534	0.0626
2(C)	0.0506	0.1133	0.0151	0.0355	0.0627	0.0491	0.0272
3(C)	0.0250	0.0253	0.0473	0.0223	0.0503	0.0363	0.0280
4(C)	0.0453	0.1293	0.0118	0.0335	0.0839	0.0587	0.0504
5(C)	0.0483	0.0312	0.0592	0.0109	0.0171	0.0140	0.0062
6(C)	0.0238	0.0402	0.0151	0.0088	0.0164	0.0126	0.0077
7(C)	0.0619	0.0085	0.0842	0.0224	0.0703	0.0463	0.0480
8(C)	0.0867	0.1347	0.0367	0.0500	0.0480	0.0490	0.0021
9(C)	0.0224	0.0501	0.0473	0.0249	0.0725	0.0487	0.0476
10(N)	0.1866	0.2532	0.1205	0.0661	0.0666	0.0663	0.0005
11(N)	0.0960	0.1287	0.0345	0.0615	0.0327	0.0471	0.0288
12(C)	0.0376	0.0326	0.0450	0.0074	0.0050	0.0062	0.0024
13(C)	0.0862	0.0938	0.0783	0.0079	0.0076	0.0077	0.0003
14(H)	0.0355	0.0294	0.0471	0.0116	0.0061	0.0088	0.0056
15(H)	0.0378	0.0214	0.0483	0.0105	0.0164	0.0135	0.0059
16(H)	0.0306	0.0228	0.0398	0.0092	0.0078	0.0085	0.0015
17(C)	0.0560	0.0584	0.0462	0.0098	0.0024	0.0061	0.0074
18(H)	0.0352	0.0275	0.0447	0.0095	0.0077	0.0086	0.0018
19(C)	0.0580	0.0613	0.0422	0.0157	0.0033	0.0095	0.0124
20(H)	0.0275	0.0309	0.0321	0.0045	0.0033	0.0006	0.0078
21(H)	0.0256	0.0192	0.0368	0.0112	0.0064	0.0088	0.0048
22(C)	0.0070	0.0087	0.0077	0.0147	0.0017	0.0082	0.0130
23(H)	0.0252	0.0183	0.0364	0.0113	0.0068	0.0091	0.0044
24(H)	0.0253	0.0229	0.0347	0.0095	0.0024	0.0059	0.0071
25(N)	0.1045	0.1078	0.0002	0.1043	0.0032	0.0538	0.1011
26(H)	0.0288	0.0298	0.0431	0.0143	0.0009	0.0067	0.0152
27(H)	0.0281	0.0254	0.0450	0.0170	0.0027	0.0098	0.0143
28(C)	0.0060	0.0067	0.0082	0.0142	0.0006	0.0074	0.0136
29(C)	0.0907	0.0939	0.0778	0.0129	0.0032	0.0081	0.0097
30(H)	0.0301	0.0304	0.0427	0.0126	0.0004	0.0061	0.0129
31(H)	0.0142	0.0130	0.0416	0.0273	0.0012	0.0143	0.0261
32(H)	0.0309	0.0277	0.0422	0.0113	0.0031	0.0072	0.0081
33(H)	0.0304	0.0252	0.0496	0.0192	0.0053	0.0122	0.0139
34(H)	0.0286	0.0249	0.0394	0.0108	0.0037	0.0073	0.0071
35(C)	0.0074	0.0085	0.0071	0.0145	0.0011	0.0078	0.0135
36(C)	0.0891	0.0898	0.0801	0.0090	0.0007	0.0048	0.0083
37(H)	0.0308	0.0245	0.0478	0.0170	0.0063	0.0117	0.0107
38(H)	0.0121	0.0127	0.0394	0.0273	0.0006	0.0133	0.0280
39(H)	0.0325	0.0285	0.0436	0.0111	0.0040	0.0075	0.0071
40(H)	0.0325	0.0279	0.0499	0.0174	0.0046	0.0110	0.0128
41(H)	0.0278	0.0339	0.0320	0.0042	0.0061	0.0010	0.0103
42(H)	0.1155	0.0968	0.1361	0.0207	0.0187	0.0197	0.0020
43(H)	0.0491	0.0132	0.0687	0.0196	0.0359	0.0277	0.0163
44(H)	0.0420	0.0049	0.0537	0.0117	0.0371	0.0244	0.0254
45(H)	0.0539	0.0150	0.0718	0.0179	0.0389	0.0284	0.0209
46(H)	0.0384	0.0072	0.0557	0.0174	0.0311	0.0243	0.0137
47(H)	0.0424	0.0020	0.0628	0.0205	0.0403	0.0304	0.0199
48(Cl)	0.0690	0.1597	0.0121	0.0569	0.0907	0.0738	0.0338

Fig. 8. (a) Chemical structure of CQP; (b) LBO analysis of CQP molecule; (c) Hirshfeld charge and Fukui index of CQP; (d) HOMO and LUMO distributions on CQP; (e)Proposed degradation pathways of CQP in Co/NC-74/PMS system.

3.6. Toxicity assessment

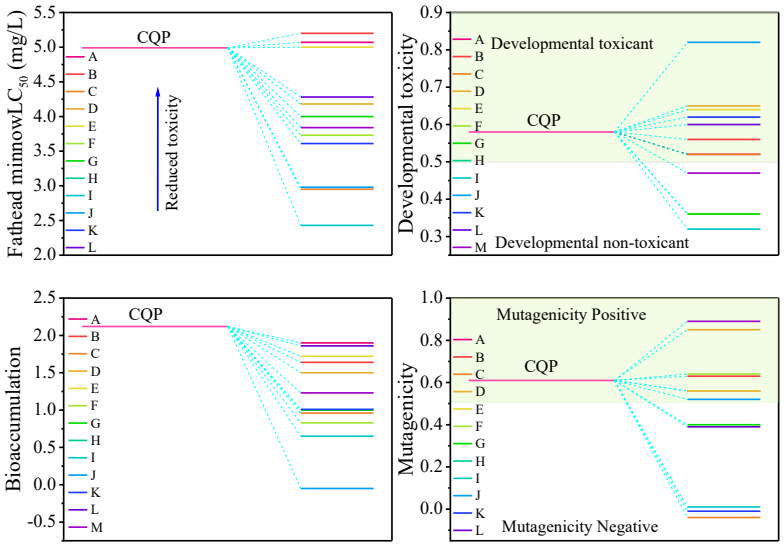


Fig. 9. (a) The acute toxicity of CQP, The predicted values for developmental toxicity (b), mutagenicity (c) and bioaccumulation factor (d).

Furthermore, the bioaccumulation factor, Daphnia magna acute toxicity, developmental toxicity, and mutagenicity of CQP and its degradation intermediates were assessed using the Toxicity Estimation

Software Tool (T.E.S.T.). Toxicity tests using Daphnia magna as a model organism showed a progressive decline, indicating that the toxicological impact of CQP and its intermediates gradually weakened throughout the degradation process (Fig. 9a). Developmental toxicity evaluation revealed that some intermediates exhibited higher developmental toxicity than CQP, which was primarily attributed to the presence of benzene ring structures in those compounds [49,50]. Meanwhile, the bioaccumulation factors of all CQP intermediates were lower than that of the parent compound, and the overall toxicity of the degradation intermediates was reduced compared to CQP. Mutagenicity assessment indicated that major intermediates were classified as "mutagenicity negative" (Fig. 9d). Notably, most intermediates showed lower developmental toxicity and mutagenicity than CQP itself, suggesting that the degradation process significantly reduced these hazards. In summary, although the degradation of P-Nip generated certain intermediate products, the overall trend indicated a reduction in key toxicity endpoints, supporting the decreased environmental risk after treatment.

4. Environmental application value

4.1. Effects of inorganic ions on CQP Degradation

The typical cations and anions were existed in the water matrix, which included the Na^+, K^+, Zn^{2+}, Ca^{2+}, Cu^{2+}, Mg^{2+}, Cl^-, HPO_4^{2-}, HPO_4^{2-}, NO_3^-, SO_4^{2-}, and HCO_3^- [51,52]. The coexisted inorganic anions have been confirmed that evident influenced on the PMS involved process. Herein, we have evaluated the influence of common positive ions on CQP Degradation. As seen from Fig. 10 a, the K^+ have a significant negative impact on the CQP Degradation. The inhibitory effect of the other metal ions was not observed in this Co/NC-74/PMS system. In general, Cl^-, NO_3^-, SO_4^{2-}, HPO_4^{2-}, and HPO_4^{2-} have notably decreased the degradation efficiency of CQP (Fig. 10b). It is widely known that the coexistence of these negative ions can resulted in a certain degree of inhibitory effect on the PMS-based process since they could react with the ROSs ($SO_4^{\bullet -}$/•OH/$^1O_2$ and $O_2^{\bullet -}$) to generate other species with lower redox potential or quench these radicals [53].

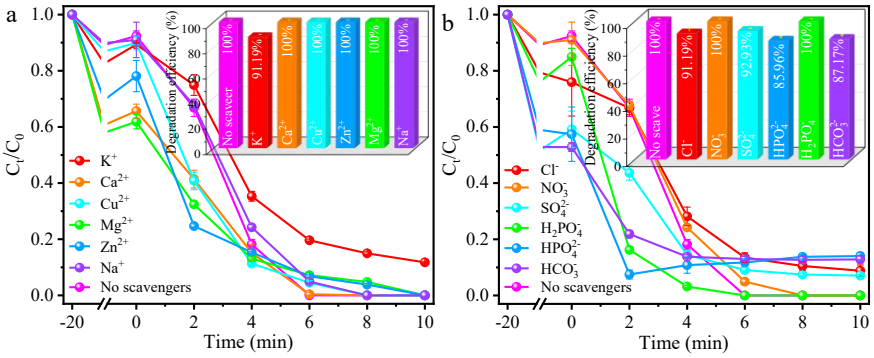


Fig. 11. Factors of the cations (a) and anions (b) on the CQP degradation efficiency in Co/NC-74/PMS system.

4.2. Effects of water matrices on CQP Degradation

In practical applications, evaluating the degradation performance in various natural water sources is essential to assess the universality of the system for removing other dyes and antibiotics [54,55]. Here, tap water (Ta-W), river water (Ri-W), and reservoir water (Re-W) were selected as simulated wastewater matrices, while deionized water (De-W) served as the control throughout the experiments. The degradation of several target pollutants (CQP, TC, DH, OTC, CR, MO, MY, and MB) were investigated (Fig. 11a). The corresponding degradation efficiencies are summarized in Table 2S. Compared with De-W and Ta-W, Re-W and Ri-W exhibited a slight inhibitory effect on the degradation of certain pollutants, such as CQP, TC, and OTC. This can be mainly attributed to the presence of various inorganic ions in natural water, which may interfere with the degradation

process. Furthermore, given that real wastewater typically contains multiple organic pollutants, it is meaningful to evaluate the system's performance in degrading mixed pollutant solutions. Similarly, mixtures of dyes (CR, MO, MY, and MB) were also efficiently decomposed in natural water matrices. As shown in Fig. 11b, the characteristic UV-Vis peaks of the antibiotic mixture (CQP, TC, DH, and OTC) decreased significantly within 10 min, indicating effective catalytic degradation.However, although antibiotics and dyes were converted into intermediates (Fig. 11c), enhancing the mineralization capacity during photocatalytic CQP degradation over Co/NC-74 remains an urgent challenge to be addressed.

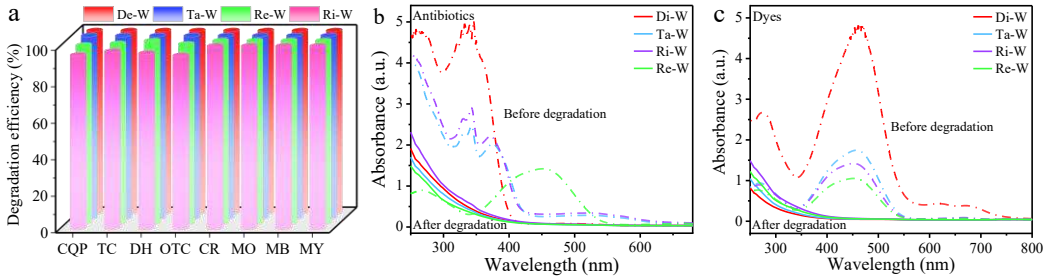


Fig. 12. The degradation efficiency of (a)multiple organic pollutants, antibiotics (b) and dyes mixtures (c) in natural water.

4.3. Effects of light irradiation and reusability on degradation of CQP

In practical applications, it is very important to further evaluate effects of the light source on the CQP degradation [56]. It is necessary to evaluate the removal efficiency of CQP under sunlight since the Xenon lamp source was used through the whole degradation process. The degradation efficiency of CQP under sunligh and Xenon lamp was equal at 10 min, indicating that the light source has a little influence on the CQP degradation. The results suggested that Co/NC-74 has great value of application. Reusability was also an important parameter in practical applications, so it is necessary to further investigate the recycling performance of catalyst. Co/NC-74 was collected and dried after the photodegradation experiment (Fig. 12). Moreover, the recycling experiment of Co/NC-74 was carried out under the same condition. The degradation efficiency still maintained at 92.8% after the six cycles. The perfect reusability of Co/NC-74 may be due to the ultrafine cobalt nanoparticles. Compared with the recently published works, 50 mg/L of CQP can be degraded within 6 min in Table 1, the concentration of organic pollutants is the highest and the consumption time is the least.

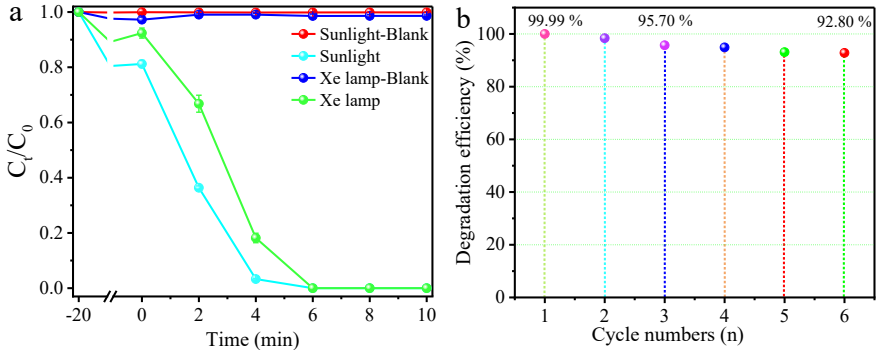


Fig. 13. The effect of light source on the CQP degradation and recycling experiments of Co/NC-74.

Table 1. The degradation of CQP recently published.

Catalyst	Poll. Conc. (mg/L)	Time (min)	Oxidants species	Oxidants quantity	D (%)	Cycle times	Ref.

O_V-BM-25	10	60	H_2O_2	1.96 mM	97.8%	5	1
O-MoS_{2-X}	10	10	H_2O_2	0.4 mM	99.5%	10	2
LaCoCuO-CeO_2	20	8	PMS	1.0 mM	100%	5	3
C_3N_4 NT	10	32	PMS	0.8 mM	93.8%	-	4
Co-N-C	10	10	PMS	1.0 mM	98.0%	5	5
Co@NC	50	6	PMS	20 mg	99.98%	5	This work

LDH., Layered double hydroxides; LaCoCuO-CeO_2, $LaCo_{0.5}Cu_{0.5}O_3$-CeO_2; PMS., Peroxymonosulfate; PS., Persulfate; Poll. Conc., Pollutants concentration; D., Degradation; Ref., Reference; —., No report.

4.4. Economic analysis

To further assess its economic feasibility of Co@NC, we calculated the cost of Co@NC including the chemical reagent cost, raw materials, and energy cost. According to the current market prices, the unit costs for $Co(NO_3)_2 \cdot 6H_2O$ and white radish are \$48.28/Kg and \$142.85/Kg, respectively. The conversion efficiency of Co-based biochar and the composites were 60 %. To produce 1 kg of Co@NC-74, the calculated amounts of white radish and $Co(NO_3)_2 \cdot 6H_2O$ are 36.0 kg, 2.037 kg, respectively. The energy cost is mainly generated from the water bath, the forced-air drying oven, freeze drying, and the tube furnace (Table 3S). The total energy cost was calculated at \$3.43/kg. The cost of this catalyst is significantly lower than the activated carbon (\$10/kg), which indicate that Co@NC-74 has strong economic viability [57].

5. Conclusion

Due to the inspiration from kimchi, Co/NC-74 was prepared with turnip. The plant cell was firstly used as a temple to construct the size-controlled Co nanoparticles to activate PMS for removing CQP. In addition, the best-performing sample Co/NC-74 can reach 99.99 % of degradation efficiency under xenon lamp and solar light irradiation. Radical trapping tests and EPR detection confirmed that the •OH, $^1O_2$ and $O_2^{\bullet -}$ play the dominant role rather than $SO_4^{\bullet -}$ for CQP degradation in Co/NC-74/PMS/vis system. Furthermore, the degradation efficiency of CQP, TC, DH, OTC, CR, MO, and MB in natural water was higher than 94 %. The water matrices have obvious impact on the CQP degradation. More importantly, the Cl^-, NO_3^-, SO_4^{2-}, HPO_4^{2-}, and HPO_4^{2-} have notable inhibition effects. The antibiotics and dyes mixture can be decomposed after 10 min. Meanwhile, 92.80 % of degradation efficiency still preserved after the 6th run, indicating the excellent reusability. Lastly, the CQP degradation pathway in Co/NC-74/PMS system was proposed and the toxicity of each intermediate were evaluated. Overall, this work was a new vision for enhancing the PMS activation efficiency.

Data availability statement

Data supporting the findings of this study are available from the corresponding author upon reasonable request.

Declarations

Competing interests The authors declare that they have no known competing financial interests or personal relationships that could have appeared to influence the work reported in this paper.

Ethical Approval We affirm that all authors adhere completely to ethical standards.

References

[1] J. Li, M. Zhu, M. Chen, Q. Mei, W. Chen, Y. Tang, Q. Wang, Natural redox mediator anthraquinone aloe-emodin facilitated the in-situ mineralized γ-FeO(OH) membrane for the removal of tannic acid through photocatalytic-PMS activation, J. Hazard. Mater. 478 (2024) 135464.

[2] Z. Cao, Y. Jia, Q. Wang, H. Cheng, High-efficiency photo-Fenton Fe/g-C_3N_4/kaolinite catalyst for tetracycline hydrochloride degradation, Appl. Clay Sci 212 (2021) 106213.

[3] L. Li, X. Yuan, Z. Zhou, R. Tang, Y. Deng, Y. Huang, S. Xiong, L. Su, J. Zhao, D. Gong, Research progress of photocatalytic activated persulfate removal of environmental organic pollutants by metal and nonmetal based photocatalysts, J. Clean. Prod. 372 (2022)133420-133441.

[4] L. Yang, Z. Wei, Z. Guo, M. Chen, J. Yan, L. Qian, L. Han, J. Li, M. Gu, Significant roles of surface functional groups and Fe/Co redox reactions on peroxymonosulfate activation by hydrochar-supported cobalt ferrite for simultaneous degradation of monochlorobenzene and p-chloroaniline, J. Hazard. Mater. 445 (2023) 130588-130602.

[5] X. Ji, J. W. Huang, W. J. Liu, H. Q. Yu, Pyrolysis of Biomass Wastes to N-Doped Biochar-Stabilized Co Nanoparticles for Efficient Pollutant Degradation Via Peroxymonosulfate Activation, ACS ES&T Eng. 1 (2021) 1715-1724.

[6] D. Li, L. Sun, R. He, G. Xiao, D. Zhu, W. Wang, J. Ye, Hierarchically porous MgO/biochar composites for efficient CO_2 capture: Structure, performance and mechanism, Chem. Eng. J 498 (2024) 155607-155618.

[7] Z. Y. Choong, M. F. Gasim, K. Y. A. Lin, T. S. Hamidon, H. Hussin, W. D. Oh, Unravelling the formation mechanism and performance of nitrogen, sulfur codoped biochar as peroxymonosulfate activator for gatifloxacin removal, Chem. Eng. J 451 (2023)138958-138972.

[8] J. Liu, S. Huang, T. Wang, M. Mei, S. Chen, J. Li, Peroxydisulfate activation by digestate-derived biochar for azo dye degradation: Mechanism and performance, SEP PURIF TECHNOL 279 (2021) 119687-119686.

[9] X. Zhang, Z. Ding, J. Yang, L. Cizmas, E. Lichtfouse, V. K. Sharma, Efficient microwave degradation of humic acids in water using persulfate and activated carbon, Environ. Chem. Lett 16 (2018) 1069-1075.

[10] X. Huang, Z. Yu, Y. Shi, Q. Liu, S. Fang, Highly efficient activation of peroxymonosulfate by Co, S co-doped bamboo biochar for sulfamethoxazole degradation: Insights into the role of S, Environ. Chem. Eng 10 (2022) 108380-108392.

[11] S. Xiong, Y. Deng, D. Gong, R. Tang, J. Zheng, L. Li, Z. Zhou, L. Su, C. Liao, L. Yang, Magnetically modified in-situ N-doped Enteromorpha prolifera derived biochar for peroxydisulfate activation: Electron transfer induced singlet oxygen non-radical pathway, Chemosphere 284 (2021) 131404-131414.

[12] X. Zhang, W. Gu, D. Liu, L. Zhou, N. N. Huy, L. Wang, J. Zhang, Y. Liu, J. Lei, Fe(II) and Pyridinic N complex sites synergy to activate PMS for specific generation of $^1O_2$ to degrade antibiotics with high efficiency, Sci Total Env 892 (2023) 164067-164077.

[13] S. Ye, G. Zeng, X. Tan, H. Wu, J. Liang, B. Song, N. Tang, P. Zhang, Y. Yang, Q. Chen, X. Li, Nitrogen-doped biochar fiber with graphitization from Boehmeria nivea for promoted peroxymonosulfate activation and non-radical degradation pathways with enhancing electron transfer, Appl. Catal. B-Environ 269 (2020) 118850-118891.

[14] H. Xu, Y. Zhang, J. Li, Q. Hao, X. Li, F. Liu, Heterogeneous activation of peroxymonosulfate by a biochar-supported Co_3O_4 composite for efficient degradation of chloramphenicols, Environ. Pollut. 257 (2020) 113610-113617.

[15] Z. Li, S. Yuan, X. Liu, Z. Rui, S. Li, S. Liu, X. Qi, Z. Wu, CoSe as highly efficient catalyst for photo-assisted activation of peroxymonosulfate for rapid degradation of phenazopyridine hydrochloride, J. Mater. Sci. Mater. 34 (2023) 1378-1381.

[16] C. Wang, S. Adhikari, Y. Li, M. Wen, Y. Wang, Highly selective zinc ion removal by the synergism of functional groups and defects from N, S co-doped biochar, SEP PURIF TECHNOL 354 (2025) 129446-129457.

[17] Y. Zhang, T. Hu, S. Hu, J. Zhang, M. Wang, M. Zhou, Z. Hou, B. He, Y. Liu, Nitrogen and Oxygen Codoped Hierarchically Porous Carbon Derived from Tannic Acid and Reed Straw for High-Performance Supercapacitors, ACS Appl Energy Mater 7 (2024) 7701-7711.

[18] X. Hu, Y. Li, X. Wei, L. Wang, H. She, J. Huang, Q. Wang, Preparation of double-layered Co-Ci/NiFeOOH co-catalyst for highly meliorated PEC performance in water splitting, Adv Powder Mater 1 (2022) 100024-100033.

[19] L. Zhao, J. Zhang, Z. Zhang, T. Wei, J. Wang, J. Ma, Y. Ren, H. Zhang, Co_3O_4 crystal plane regulation to efficiently activate peroxymonosulfate in water: the role of oxygen vacancies, J. Colloid Interface Sci. 623 (2022) 520–531.

[20] H. Wang, D. Wang, C. Sun, X. Zhao, C. Xu, Z. Li, Y. Hou, L. Lei, B. Yang, X. Duan, Oriented generation of $^1O_2$ from peroxymonosulfate via Co_3O_4 facet engineering, App. Catal. B: Environ. 364 (2025) 124854.

[21] Y. Zhao, L. Wu, P. Hong, X. He, S. Gao, Y. Yu, B. Liao, H. Pang, Ultrathin CoO@NC nanosheets derived from $NaBH_4$-treated ZIF-67 for ofloxacin degradation, Appl. Surf. Sci 645, (2024) 158864-158873.

[22] A. Xie, X. Tai, Y. Guo, J. Miao, D. Liu, R. Zhang, L. Cheng, Z. Zhao, Y. Tang, X. Yang, J. Pan, P. Wan, Elaborate construction of honeycomb-like porous carbon with embedment of N-doped carbon nanotubes as efficient electrocatalyst for zinc-air battery, Carbon 228 (2024) 119299-119310.

[23] Y. Luo, H. Han, G. Zhang, Q. Wang, Y. Jia, Construction of Z-scheme α-Fe_2O_3/graphene/Bi_2O_2S heterojunction for visible-light-driven photocatalytic CO_2 conversion, SEP PURIF TECHNOL 314 (2023)123607-123619.

[24] Z. Li, X. Zhang, G. Li, F. Han, D. Hu, X. Huang, H. Yuan, Y. Tan, Hollow Co/CoO/Carbon nanofibers promoted PMS decomposition for the degradation of Rhodamine B, Mater. Sci. Technol 157 (2023) 120-129.

[25] W. Zhang, M. Li, W. Shang, M. Wang, J. Zhang, F. Sun, M. Li, X. Li, Singlet oxygen dominated core-shell Co nanoparticle to synergistically degrade methylene blue through efficient activation of peroxymonosulfate, SEP PURIF TECHNOL 308 (2023) 122849-122860.

[26] Y. Li, Q. An, Z. Xiao, K. Zhu, X. Zhang, C. Wang, Y. Liu, S. Zhai, 3D hollow cobalt/carbon fiber-like PMS activator for dynamic carbamazepine degradation: promotional effect and reaction mechanism, Chem. Eng. J 487 (2024) 150636-150645.

[27] X. Fu, L. Wang, Z. He, Y. Gao, Y. Xia, J. Tao, Z. Zhao, Synergetic interfacial charge transfer with Z-scheme heterostructure and S–Mo–S linkage in one-pot synthesized $SnIn_4S_8$/MoS_2 for efficient photocatalytic activity, J. Solid State Chem. 319 (2023) 123794-123804.

[28] K. L. Oguzie, M. Qiao, X. Zhao, E. E. Oguzie, V. O. Njoku, G. A. Obodo, Oxidative degradation of Bisphenol A in aqueous solution using cobalt ion-activated peroxymonosulfate, J. Mol. Liq. 313 (2020) 113569-113576.

[29] H. Huang, M. Sun, S. Li, S. Zhang, Y. Lee, Z. Li, J. Fang, C. Chen, Y. X. Zhang, Y. Wu, Y. Che, S. Qian, W. Zhu, C. Tang, Z. Zhuang, L. Zhang, Z. Niu, Enhancing H_2O_2 Electrosynthesis at Industrial-Relevant Current in Acidic Media on Diatomic Cobalt Sites, J Am Chem Soc 146 (2024) 9434-9443.

[30] X. Fu, L. Wang, F. Gao, C. Zhu, J. Tao, Z. He, Y. Xia, Z. Zhang, Insight into the synergic charge

transfer on S-Mo bond-modified Z-scheme $MgIn_2S_4/MoSe_2$ towards norfloxacin degradation Mechanism, pathways and toxicity evaluation, Fuel. 368 (2024) 131700.

[31] Y. Huang, J. Zou, J. Lin, H. Yang, M. Wang, J. Li, W. Cao, B. Yuan, J. Ma, ABTS as Both Activator and Electron Shuttle to Activate Persulfate for Diclofenac Degradation: Formation and Contributions of ABTS$\bullet^+$, $SO_4\bullet^-$, and •OH, Environ Sci Technol 57 (2022) 18420-18432.

[32] B. Li, B. Chen, Z. Wei, Challenging established norms: The unanticipated role of alcohols in UV/PDS radical quenching, J. Hazard. Mater. 478 (2024) 135502-135502.

[33] Q. Yang, X. Niu, Y. Zhu, Y. Cui, Y. Chao, P. Liang, C. Zhang, S. Wang, Modulating anion defect in $La_{0.6}Sr_{0.4}Co_{0.8}Fe_{0.2}O_{3-\delta}$ for enhanced catalytic performance on peroxymonosulfate activation: Importance of hydrated electrons and metal-oxygen covalency, J. Hazard. Mater. 432 (2022) 128686-128699.

[34] C. Zhu, X. Fu, L. Wang, J. Yan, Z. He, Y. Xia, W. Lian, H. Zhang, T. Yang, Y. Gao, Design of S-O "highway" at Z-scheme heterojunction interface for efficient degradation treatment of lomefloxacin and actual pharmaceutical wastewater, J. Environ, Manage. 389 (2025) 126160.

[35] X. Fu, L. Wang, F. Gao, C. Zhu, J. Tao, Z. He, Y. Xia, Z. Zhang, Insight into the synergic charge transfer on S-Mo bond-modified Z-scheme $MgIn_2S_4/MoSe_2$ towards norfloxacin degradation Mechanism, pathways and toxicity evaluation, Fuel. 368 (2024) 131700.

[36] G. Li, T. Qiu, Q. Wu, Z. Zhao, L. Wang, Y. Li, Y. Geng, H. Tan, Pyrene-Alkyne-Based Conjugated Porous Polymers with Skeleton Distortion-Mediated $\bullet O_2^-$ and $^1O_2$ Generation for High-Selectivity Organic Photosynthesis, Angew. Chem. - Int. Ed. 63 (2024) 202405396.

[37] K. Chen, Q. Tang, C. Dong, G. Zhang, J. Zhao, Y. Chen, P. Xiao, Carbon nanotube supported cobalt nickel sulphide nano-catalyst for degradation of chloroquine phosphate with peroxymonosulphate, Environ. Technol. 45 (2023) 5465-5482.

[38] X. Peng, J. Wu, Z. Zhao, X. Wang, H. Dai, Y. Wei, G. Xu, F. Hu, Activation of peroxymonosulfate by single atom Co-N-C catalysts for high-efficient removal of chloroquine phosphate via non-radical pathways: Electron-transfer mechanism, Chem. Eng. J 429 (2022) 132245-132257.

[39] J. Shi, T. Yang, T. Zhao, K. Pu, J. Shi, A. Zhou, H. Li, S. Wang, J. Xue, Insights on the efficiency and contribution of single active species in photocatalytic degradation of tetracycline: Priority attack active sites, intermediate products and their toxicity evaluation, J. Environ. Manage. 367 (2024) 121970-121987.

[40] L. Zhao, S. Pan, N. Holzmann, P. Schwerdtfeger, G. Frenking, Chemical Bonding and Bonding Models of Main-Group Compounds, Chem. Rev. 119 (2019) 8781-8845.

[41] A. H. Radhi, HOMO-LUMO Energies and Geometrical Structures Effecton Corrosion Inhibition for Organic Compounds Predict by DFT and PM3 Methods. NeuroQuantology 18, (2020) 37-45.

[42] L. Wang, J. Wei, J. Huo, W. Ji, X. Zhang, Y. Li, J. Li, N. Cui, W. Yan, Y. Zhao, J. Li, Harnessing electronically core-shell CoFe alloy-carbon from Prussian blue analogues for efficient pollutant abatement via peracetic acid activation: Dual reactive species generation and synergistic mechanisms, Appl. Catal. B: Environ. 371 (2025) 125284.

[43] S. K. Alghamdi, F. Abbas, R. K. Hussein, A. G. Alhamzani, N. T. El-Shamy, Spectroscopic characterization (IR, UV-Vis), and HOMO-LUMO, MEP, NLO, NBO Analysis and the Antifungal Activity for 4-Bromo-N-(2-nitrophenyl) benzamide; Using DFT Modeling and In silico Molecular Docking, J. Mol. Struct. 1271 (2023) 134001-134010.

[44] A. Saral, P. Sudha, S. Muthu, A. Irfan, Spectroscopic profiling, DFT computations, molecular docking and molecular dynamic simulation of biologically active 5-isoquinolinesulfonic acid, J

BIOMOL STRUCT DYN 41 (2021) 722-735.

[45] P. Gao, Y. Q. Liu, W. Xiao, F. Xia, J. Y. Chen, L. W. Gu, F. Yang, L. H. Zheng, J. Z. Zhang, Q. Zhang, Z. J. Li, Y. Q. Meng, Y. P. Zhu, H. Tang, Q. L. Shi, Q. Y. Guo, Y. Zhang, C. C. Xu, L. Y. Dai, J. G. Wang, Identification of antimalarial targets of chloroquine by a combined deconvolution strategy of ABPP and MS-CETSA, Mil. Med. Res 9 (2022) 30-44.

[46] T. Huang, F. Tian, Z. Wen, G. Li, Y. Liang, R. Chen, Synergistic mediation of metallic bismuth and oxygen vacancy in Bi/Bi_2WO_{6-x} to promote $^1O_2$ production for the photodegradation of bisphenol A and its analogues in water matrix, J. Hazard. Mater. 403 (2021) 123661-123670.

[47] J. Sun, D. Zhang, D. Xia, Q. Li, Orange peels biochar doping with Fe-Cu bimetal for PMS activation on the degradation of bisphenol A: A synergy of $SO_4\bullet^-$, •OH, $^1O_2$ and electron transfer, Chem. Eng. J. 471 (2023) 144832-144846.

[48] P. Gao, Y. Q. Liu, W. Xiao, F. Xia, J. Y. Chen, L. W. Gu, F. Yang, L. H. Zheng, J. Z. Zhang, Q. Zhang, Z. J. Li,. Identification of antimalarial targets of chloroquine by a combined deconvolution strategy of ABPP and MS-CETSA, Mil. Med. Res. 9 (2022)30.

[49] X. Fu, C. Zhu, J. Yan, X. Lu, Z. He, Y. Xia, W. Lian, Q. Wu, J. Chen, J. Pu, T. Yang, Y. Gao, "Three-in-one": Triple-engineered charge transfer in $Bi_4O_5Br_2/FeS_2$ hybrid for efficient treatment of cefalexin and real pharmaceutical wastewater, Chem. Eng. J. 523 (2025) 168514.

[50] H. Dai, W. Luo, L. Jin, L. Deng, Q. Wang, J. Hu, R. P. Singh, Degradation of chloroquine phosphate during UV/H_2O_2 process: Performance, kinetics, and degradation pathways, J. Environ. Chem. Eng. 12 (2024) 112493-112502.

[51] K. Chen, Q. Tang, C. Dong, G. Zhang, J. Zhao, Y. Chen, P. Xiao, Carbon nanotube supported cobalt nickel sulphide nano-catalyst for degradation of chloroquine phosphate with peroxymonosulphate, Environ. Technol. 45 (2024) 5465-5482.

[52] Y. Wan, H. Luo, Y. Cai, Z. Dang, H. Yin, Selective removal of total Cr from a complex water matrix by chitosan and biochar modified-FeS: Kinetics and underlying mechanisms, J. Hazard. Mater. 454 (2023) 131475.

[53] W. Song, Z. Yu, H. Li, Y. Ji, L. Cao, L. Ren, X. Li, Y. Li, X. Xu, L. Yan, Insights into the factors influencing the oxidation of antibiotic pollutants in nitrogen-doped biochar/PMS system: The roles of physicochemical properties and reaction pathways, Chem. Eng. J 498 (2024) 155601.

[54] O. Alegbeleye, O. B. Daramola, A. T. Adetunji, O. T. Ore, Y. J. Ayantunji, R. K. Omole, D. Ajagbe, S. O. Adekoya, Efficient removal of antibiotics from water resources is a public health priority: a critical assessment of the efficacy of some remediation strategies for antibiotics in water, Environ Sci Pollut R 29 (2022) 56948-57020.

[55] J. Ji, H. Li, S. Liu, Current natural degradation and artificial intervention removal techniques for antibiotics in the aquatic environment: A review, Applied Sciences 15 (2025) 5182.

[56] H. Dai, W. Luo, L. Jin, L. Deng, Q. Wang, J. Hu, R. P. Singh, Degradation of chloroquine phosphate during UV/H_2O_2 process: Performance, kinetics, and degradation pathways, Environ. Chem. Eng 12 (2024) 112493.

[57] J. Sun, H. Zhou, J. Xu, M. Wang, X. Liu, X. Huang, Y. Wang, S. Bai, Z. Huang, Simple preparation of nickel single atoms for efficient CO_2 electroreduction and techno-economic analysis, Appl. Catal. B: Environ. 358 (2024)124396.

Supplementary Files

This is a list of supplementary files associated with this preprint. Click to download.

- supportinformation.docx